*Journal of Polymer Science and Engineering* 2026, 9(1), 11929.
https://doi.org/10.24294/jpse11929

Article

# The response of the composite circular diaphragms under thermo-mechanical stresses via bulge testing

**Wael A. Altabey**

Department of Mechanical Engineering, Faculty of Engineering, Alexandria University, Alexandria 21544, Egypt; wael.altabey@gmail.com

**CITATION**

Altabey W A. The response of the composite circular diaphragms under thermo-mechanical stresses via bulge testing. Journal of Polymer Science and Engineering. 2026; 9(1): 11929. https://doi.org/10.24294/jpse11929

**ARTICLE INFO**

Received: 27 November 2025
Accepted: 12 March 2026
Available online: 30 March 2026



**Abstract:** Under thermo-mechanical stress via a bulge test (BT), composite circular diaphragms (CCD) exhibit temperature-dependent mechanical behavior, including changes in Young's modulus, yield strength, and residual stress. The application of a differential pressure and temperature causes the membrane to deform, allowing researchers to characterize composite material properties, particularly for materials used in microelectromechanical sensors (MEMS) operating in harsh environments. This paper aims to explore how CCD made from basalt fiber reinforced polymer (BFRP) behaves under thermal and mechanical stress, particularly in various engineering and bioengineering sensor applications, using a technique known as the BT. To start, the diaphragm is pre-stressed and clamped between two plates. When applying differential pressure, it causes the diaphragm to deform. An analytical approach is developed for utilizing the BT to describe the thermo-mechanical properties of these diaphragms. This method is well-suited for examining how diaphragms behave mechanically in both elastic and plastic states. A finite element model (FEM) is extended to analyze the BT outcomes and look into how pre-stress influences the pressure testing, comparing results from the FEM with those derived from analytical calculations. The variations in thickness and material type are also taken into account to better understand how they affect the diaphragm's mechanical behavior under stress. Additionally, this work considers how temperature impacts the material properties of the diaphragm, which is crucial for analyzing its thermo-mechanical response. The relative ($E_r$) for maximum deflection $w_{max}$ the analytical and numerical results is less than 0.3%. The simulations are done using ANSYS, MATLAB and its PDE toolbox to get the results.

**Keywords:** composite circular diaphragms; BFRP; thermo-mechanical stress; bulge test; MEMS; FEM

## 1. Introduction and literature review

### 1.1. Introduction

The circular diaphragm plays an important role in various engineering and bioengineering sensor applications, particularly in MEMS. These sensors can be tiny, ranging from the sub-micrometer (μm) level to several millimeters (mm), like pressure sensors, where the CCD deforms in response to pressure differences. This deformation then gets converted into an electrical signal that's sent out from the sensor. Common materials for diaphragms include Bronze, Brass, Aluminum, and Stainless Steel.

#### 1.1.1. Composite materials behaviors

In the beginning, composite materials consist of three parts: the matrix, the fiber-matrix interface, and the fiber itself. They don't all fail at the same time because they have different ultimate properties. When it comes to mechanical repeating loading, such as happens to the diaphragm in bioengineering sensors and MEMS, these materials typically go through three stages before failing. Phase I is when the matrix

starts to crack, followed by Phase II, which involves local delamination that happens as the matrix cracking progresses. Finally, in Phase III, the actual rupture can be seen, which is the result of the consolidation of that local delamination. **Figure 1** shows a visual representation of this process [1,2].

These failure criteria also play a role in how to read the sensor data for signs of damage. For example, if a composite structure experiences a load that goes beyond what it is expected to handle, a sensor can pick up on changes in strain or other metrics that suggest damage has happened. **Table A1** in **Appendix A** shows the key failure criteria [3,4].

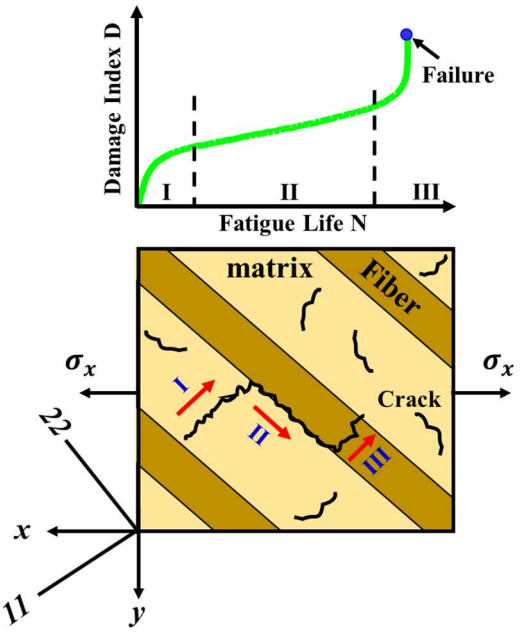


**Figure 1.** The Failure mechanisms phases.

### 1.1.2. The laminate composites test techniques

There are a couple of main ways to test laminate composites: destructive testing and non-destructive testing (NDT). Destructive testing involves various experimental methods and visual inspections on-site to evaluate samples for potential failure. This could include tests like tensile, compression, inter-laminar shear, and fracture tests. Some of the usual destructive methods for laminate composites are sectioning, bending, and fractography [5].

On the other hand, NDT techniques have been really helpful for assessing laminate composites in place, allowing us to check their structural integrity effectively [6,7]. A breakdown of the different types of NDT is shown in **Figure 2**.

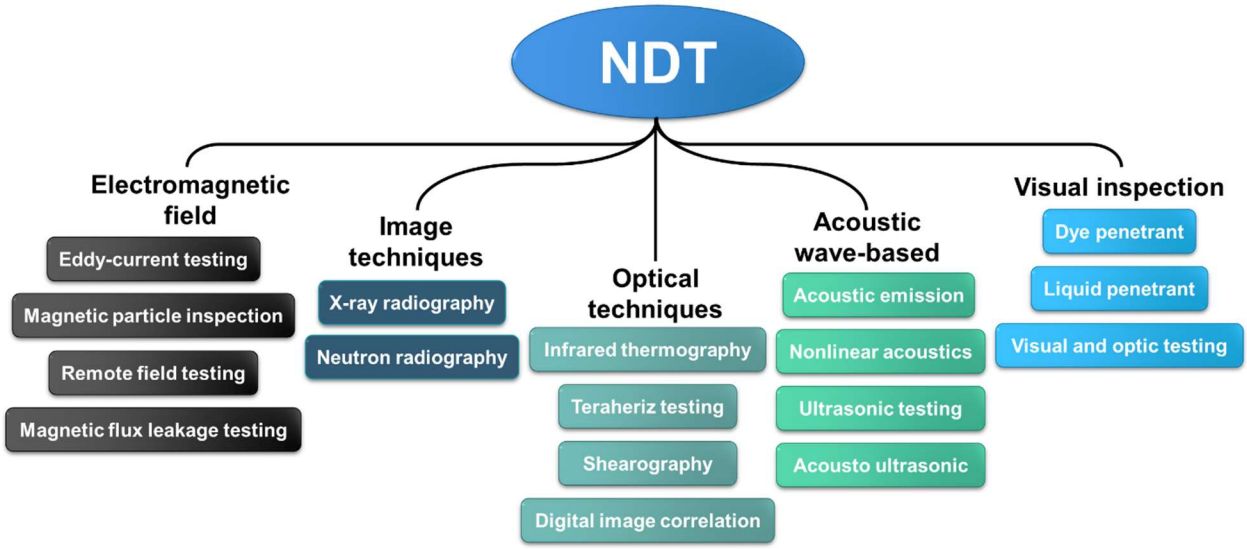


**Figure 2.** The different types of NDT in Laminate Composites.

### 1.1.3. Bulge test (BT) technique

The plane-strain BT is a useful method for figuring out the mechanical properties of thin films. Basically, it looks at how a circular membrane made from the film behaves under pressure, which helps us get the stress-strain curve for that film (**Figure 3**). With a thin membrane in plane strain, stress and strain are evenly spread out across its width, making it possible to come up with some simple formulas for both stress and strain [8,9].

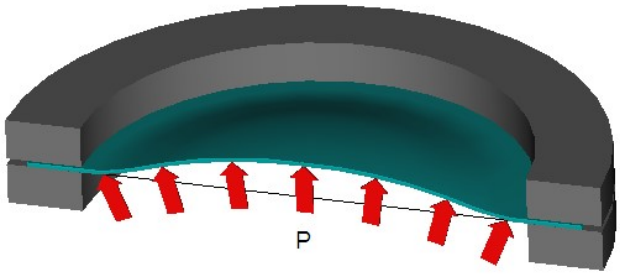


**Figure 3.** The BT Technique.

## 1.2. Literature review

When it comes to testing the mechanical properties of diaphragm materials, hydrostatic bulging of sheets, often referred to as the BT, is a distinct method. Previous research aimed at predicting how metals behave under bulging. The earliest contributions to this field can be traced back to Hill [10] and Mellor [11], who were among the first to apply the BT technique to circular diaphragms. Suleman and Bosi [12] created a detailed finite strain model to understand how inflated diaphragms deform using the BT method. They provide proof that this approach does a great job of capturing both the elastic and plastic behaviors of bilinear and nonlinear elastoplastic materials, whether at small or large plastic strains. Ashrafian and Hosseini Kordkheili [13] developed a plastic model that depends on temperature for pure aluminum diaphragms, specifically for large strains, by employing the BT method. Other researchers, Shi et al. [14], Barnwal et al. [15], and Bao et al. [16]

studied how anisotropic Aluminum sheets bulge, comparing their experimental findings with theoretical predictions.

Tian et al. [17] set up a 2D CFD model with an unsteady axisymmetric model that used overset and dynamic meshes to show the flow characteristics during the diaphragm petaling process. Currao and Hsu [18] introduced a 2D dual-diaphragm rupture model. They modeled ruptured areas as walls that fail under pressure, drawing from earlier studies on open areas. Their research suggested that if the diaphragm opens gradually, it helps reduce shock waves. Li et al. [19] used explicit dynamics to run simulations on the rupture of solid diaphragms, looking into how different shapes, pressure ratios, and temperatures affect the way these diaphragms fail.

So far, the goal of both theoretical and numerical studies has been to really nail down how metals react during hydrostatic bulging. The connections between pressure, strain, and how shapes change were figured out. Wan et al. [20] measured the residual stresses in plates or membranes that were clamped at the edges. They either applied uniform hydrostatic pressure or used a central load through a cylindrical punch. They created analytical models based on average stress in membranes and compared those with results from finite element analysis. Over the past few decades, numerical solutions have become really important in the bulging technique to figure out the mechanical properties of metals.

Since then, the focus of research on the BT has shifted to looking at how accurate and reliable it is for studying the mechanical properties of thin film materials. For instance, Jung et al. [21] reported that not considering the initial height of the membrane can lead to some misleading nonlinear elastic behavior in the film. Similarly, Yang et al. [22] examined how the initial conditions of the film, like wrinkling, residual stress, and the initial membrane height, affected their findings using finite element analyses. A lot of researchers have also taken a closer look at the accuracy and reliability of the BT [23–27]. What they've found is that while figuring out the plane-strain modulus with the plane-strain bulge equation is pretty accurate, calculating residual stress can be less dependable, especially when the levels are low. Some folks have even suggested new methods to analyze BT data to make this technique more accurate and reliable.

This paper examined the composite circular diaphragms (CCD) made from BFRP under thermo-mechanical stress via a bulge test (BT), which exhibit temperature-dependent mechanical behavior, including changes in Young's modulus, yield strength, and residual stress. The thermal behavior of BFRP is checked to determine its suitability for use in diaphragms instead of traditional materials such as aluminum and polyimide. The application of a differential pressure and temperature causes the membrane to deform, allowing the characterization of the thermomechanical properties of BFRP, and that's all the materials used in MEMS need for operating in harsh environments. The new diaphragm material has not been studied by researchers before, to the best of the author's knowledge.

## 2. Methodology

In this research, a traditional BT method to examine how CCD made from BFRP behaves under thermal and mechanical conditions is created. First off, the model will

be pre-stressed to eliminate any initial deflection before start for applying pressure to the diaphragm. After that, it's clamped between two plates, where a differential pressure ($P$) and a specific temperature ($T_b$) cause the CCD to deform. A partial differential equation tailored to the diaphragm conditions will be derived to establish an analytical solution for the bulged CCD, factoring in the effects of residual strength from pre-stressing. The thermal cumulative deterioration relationship will be plotted by deriving the thermal effect equation for BFRP materials by tracking the cumulative deterioration index of the diaphragm material, using various BFRP parameters. A FEM was also completed to plot the first four mode shapes of the CCD, and verify the accuracy of our proposed BT for CCD, and found good agreement between the FEM and analytical calculations. The simulation results were produced using ANSYS-14 and MATLAB software toolboxes. **Figure 4** illustrates the proposed method for the thermomechanical behavior methodology of CCD.

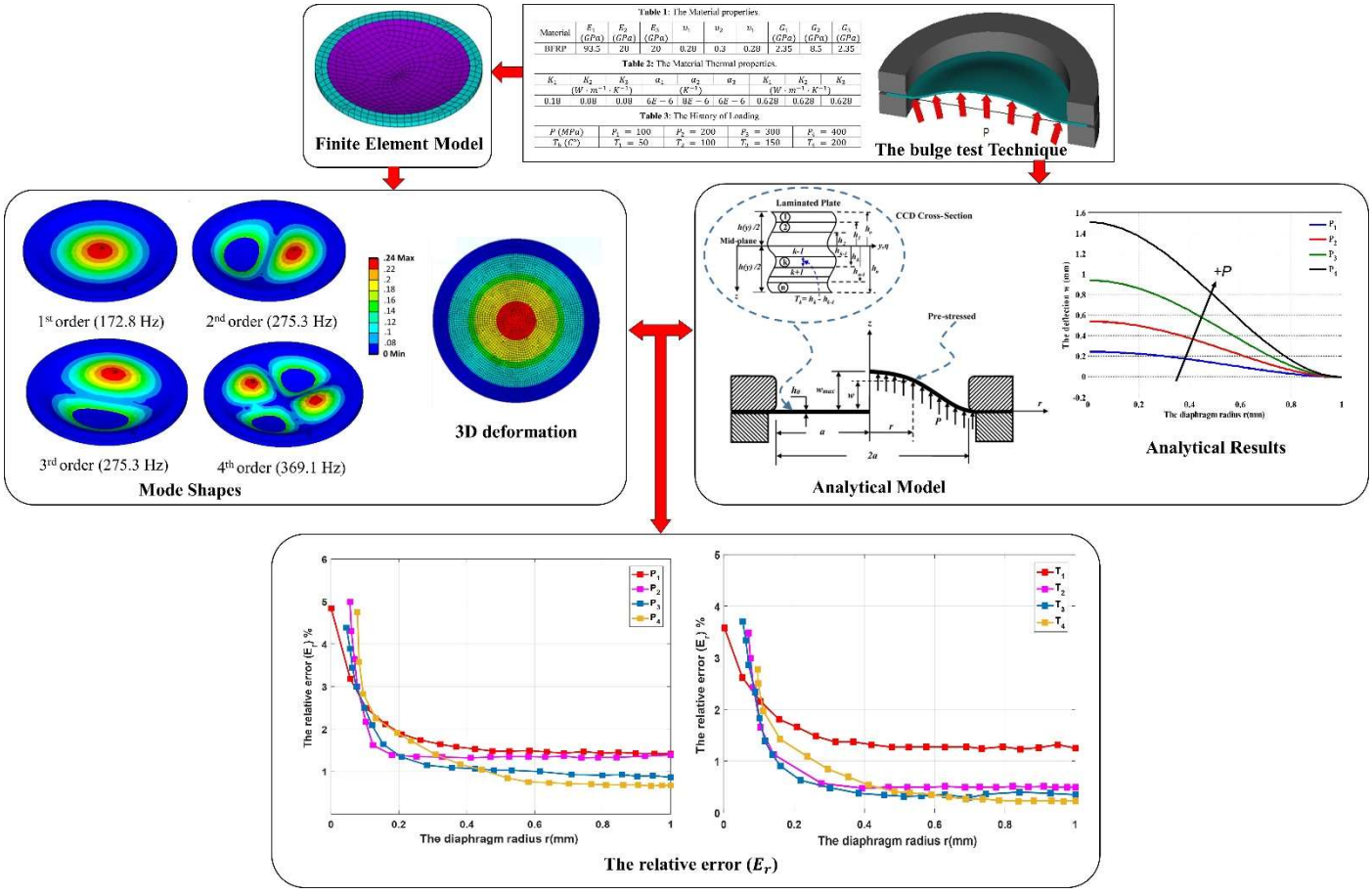


**Figure 4.** The diagram of the thermomechanical behavior methodology of CCD.

## 3. Theoretical basis

### 3.1. The assumption

1. The displacements in the $r$ and $\theta$ directions are very small, i.e., they can be neglected and the effective equation is the equation in the direction of the deflection $w$.
2. The steady state condition, i.e., the change of deflection $w$ with the time $t$ can be neglected.

3. The pre-stressed circular thin plate in the hydraulic bulge system, the in-plane loads are in $r$ and $\theta$ direction only i.e. $N_{r\theta} = 0$.
4. The plate with thickness $h$ subjected to uniform pressure load $P$.
5. The temperature $T_b$ is uniform radially $r$ but varying through thickness $h$.
6. The plate is a symmetric cross-ply laminate.

## 3.2. Mathematical model

**Figure 5a** shows the geometric model of the circular diaphragm, both before and after it has been displaced to the left and right halves. In the illustration, the film has a radius denoted as $a$ and the thickness of $h$.

First, the diaphragm gets pre-stressed with radial stress $\sigma_0$ to create an initial deflection before any load is applied, which is set to zero, and then it's clamped between two plates. The top plate is kept at room temperature, $T_t = 25$ ℃, while the underside of the film is in contact with a thermo-fluid medium at pressure $P$ and temperature $T_b$. Check out **Figure 5b** for a look at how the diaphragm deforms into a dome shape.

The motion of the circular diaphragm, based on classical deformation theory, can be described by the equation for plate deflection $w(r, \theta, t)$, is presented by Grolleau et al. [26] as:

$$\frac{\partial^2 m_r}{\partial r^2} - \frac{2}{r}\frac{\partial^2 m_{rt}}{\partial r \partial \theta} + \frac{\partial^2 m_t}{\partial \theta^2} = -\rho h \frac{\partial^2 w}{\partial t^2} \tag{1}$$

In this case, $w$ represents the transverse deflection, $\rho$ is the density per unit area of the plate, and $h$ refers to the thickness of the CCD at any given point. These values can be determined from the shape shown in **Figure 5** using the following equations:

$$h = h_0 \left(\frac{sin\,\alpha}{\alpha}\right)^2 \left(\frac{\varphi}{sin\,\varphi}\right) \tag{2}$$

$$\alpha = sin^{-1}\left(\frac{a}{R}\right) \tag{3}$$

$$\varphi = tan^{-1}\left(\frac{r}{S}\right)( \tag{4}$$

The radius of curvature, $R$, is shown in **Figure 5**.

$$R = \frac{a^2 + w_{max}}{2w_{max}} \tag{5}$$

$$S = \frac{a}{tan\,\alpha} \tag{6}$$

The moments of bending and twisting ($m_r$, $m_t$, $m_{rt}$) can be expressed along with the shear forces ($q_r$, $q_t$) in relation to displacements and the thermal effects, like this:

$$\left.\begin{aligned} m_r &= -D_{11}\frac{\partial^2 w}{\partial r^2} + \frac{1}{r^2}D_{12}\left(r\frac{\partial w}{\partial r} + \frac{\partial^2 w}{\partial \theta^2}\right) + \alpha_T\frac{\Delta T}{h} \\ m_t &= -\frac{1}{r^2}D_{11}\left(r\frac{\partial w}{\partial r} + \frac{\partial^2 w}{\partial \theta^2}\right) + D_{12}\frac{\partial^2 w}{\partial r^2} + \alpha_T\frac{\Delta T}{h} \\ m_{rt} &= m_{tr} = -D_{66}\left(\frac{1}{r}\frac{\partial^2 w}{\partial r\partial\theta} - \frac{1}{r^2}\frac{\partial w}{\partial\theta}\right) \\ q_r &= -D_{11}\frac{\partial}{\partial r}(\nabla_r^2 w) - \frac{1}{r^2}(D_{12}+4D_{66})\frac{\partial m_t}{\partial r} \\ q_t &= -\frac{1}{r^3}D_{22}\frac{1}{r}\frac{\partial}{\partial\theta}(\nabla_r^2 w) - \frac{1}{r}(D_{12}+4D_{66})\frac{\partial m_t}{\partial\theta} \end{aligned}\right\} \quad (7)$$

In the same way, the equations for the plane stress components of the CCD can be expressed like this, based on Equation (7):

$$\sigma_r = \frac{12m_r}{h^3}z,\ \sigma_t = \frac{12m_t}{h^3}z,\ \tau_{rt} = \tau_{tr} = \frac{12m_{tr}}{h^3}z( \quad (8)$$

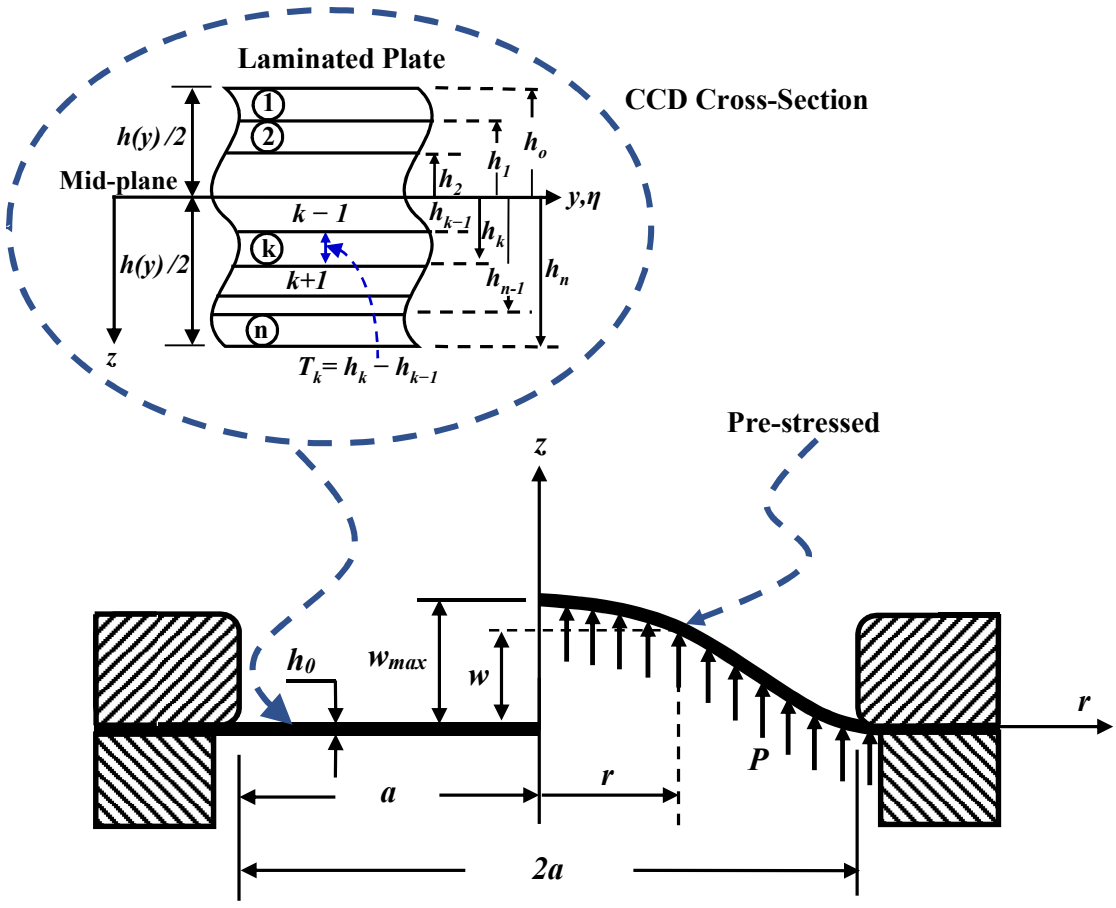


(**a**) The geometric model

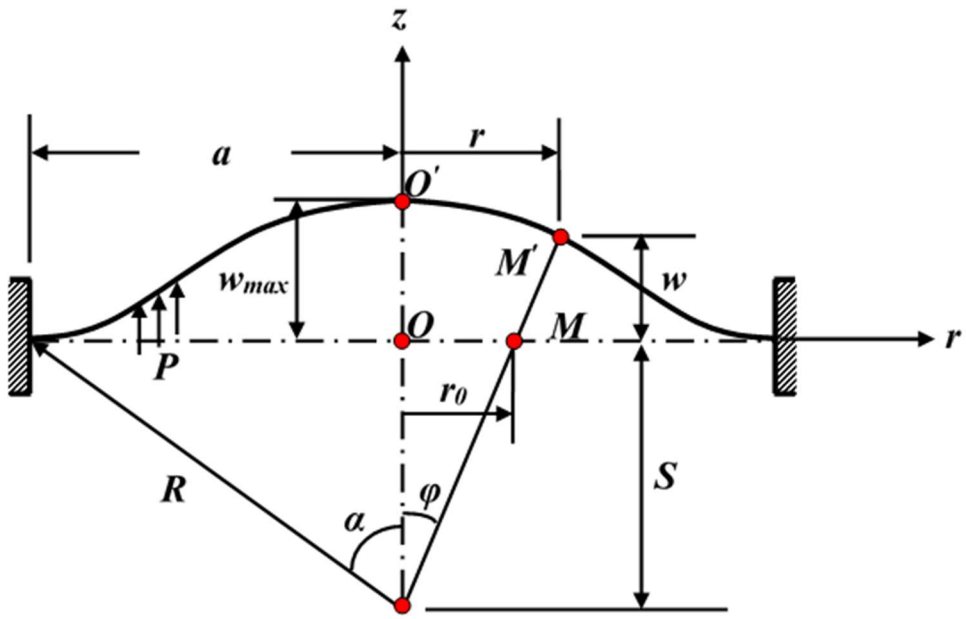


(**b**) The deformation model

**Figure 5.** The diaphragm modeling system.

The diaphragm's flexural rigidity, denoted as $D_{ij}$, is defined as:

$$D_{ij} = \frac{1}{3}\frac{h^3(y)}{h_o^3}\sum_{k=1}^{n}\left[\bar{Q}_{ij}\right]_k \left(h_{ok}^3 - h_{ok-1}^3\right), i,j = 1,2,3, \quad (9)$$

where $\bar{Q}_{ij}$ is the stiffness coefficient and can be presented in terms of the engineering notations as:

$$\bar{Q}_{ij} = \begin{bmatrix} Q_{11} & Q_{12} & Q_{13} \\ Q_{12} & Q_{22} & Q_{23} \\ Q_{13} & Q_{23} & Q_{66} \end{bmatrix} = \begin{bmatrix} \frac{E_{11}}{(1-\nu_{12}\nu_{21})} & \frac{\nu_{21}E_{11}}{(1-\nu_{12}\nu_{21})} & 0 \\ \frac{\nu_{21}E_{11}}{(1-\nu_{12}\nu_{21})} & \frac{E_{22}}{(1-\nu_{21}\nu_{12})} & 0 \\ 0 & 0 & G_{12} \end{bmatrix} \quad (10)$$

So, the main partial differential equation for the CCD, which is under thermal and mechanical loads like the one illustrated in **Figure 5**, simplifies to:

$$\nabla_r^4 w \equiv D_{11}\frac{\partial^4 w}{\partial r^4} + \frac{2}{a^2}(D_{12}+2D_{66})\frac{\partial^4 w}{\partial r^2 \partial \theta^2} + \frac{1}{a^4}D_{22}\frac{\partial^4 w}{\partial \theta^4} + N_r\frac{\partial^2 w}{\partial r^2} + \frac{1}{a^2}N_\theta\frac{\partial^2 w}{\partial \theta^2} + \frac{1}{a}N_{r\theta}\frac{\partial^2 w}{\partial r \partial \theta} = -\rho(P+P_T)\frac{\partial^2 w}{\partial t^2} \quad (11)$$

where $\bar{N}_r$, $\bar{N}_\theta$ and $\bar{N}_{r\theta}$ are in-plane force, $w$ is the diaphragm deflection. For pre-stressed diaphragm in the BT technique, the in-plane load at $r\theta$ plane is eliminated i.e., $N_{r\theta} = 0$ and divided by $\frac{D_{22}}{a^4}$, Thus, the CCD governing differential equation becomes:

$$a^4\psi_1\frac{\partial^4 w}{\partial r^4} + 2a^2\psi_2\frac{\partial^4 w}{\partial r^2 \partial \theta^2} + \frac{\partial^4 w}{\partial \theta^4} + a^4\beta_1\frac{\partial^2 w}{\partial r^2} + a^2\beta_2\frac{\partial^2 w}{\partial \theta^2} = -\Omega^2(P+P_T)\frac{\partial^2 w}{\partial t^2} \quad (12)$$

where $\psi_1 = \frac{D_{11}}{D_{22}}$, $\psi_2 = \frac{(D_{12}+2D_{66})}{D_{22}}$, $\beta_1 = \frac{N_r}{D_{22}}$, $\beta_2 = \frac{N_\theta}{D_{22}}$, $\Omega = \frac{\rho a^4}{D_{22}}$, the thermal load, denoted as $P_T$, applied to the CCD is described as follows:

$$P_T = \nabla_r^2 m_T \tag{13}$$

The equation for the operator $\nabla_r^2 = \left(\frac{\partial^2}{\partial r^2} + \frac{1}{r}\frac{\partial}{\partial r} + \frac{1}{r^2}\frac{\partial^2}{\partial \theta^2}\right)$, and the thermal equivalent bending moment, $m_T$, is calculated using this formula:

$$m_T = \alpha_T D_{66} \int_{-(h/2)}^{+(h/2)} \Delta T z dz = \alpha_T D_{66} \frac{T_t - T_b}{h_o} \tag{14}$$

The frequency parameter $(\Omega)$ in non-dimensional form can be evaluated as:

$$= \sqrt{\rho a^4 P \psi_3 \alpha_T (T_t - T_b)\omega^2} \tag{15}$$

where $\psi_3 = \frac{D_{66}}{D_{22}}$, $\omega$ is the natural frequency.

### 3.3. The Pre-stress modeling

Before applying the load on the CCD, the existing biaxial residual stress per unit length, $\sigma_0$, should take into account in the radial direction. This is important to make sure that the deflection, $w$, remains at zero, as illustrated in **Figure 6**. So, it should include this pre-stress in the radial stress equation before doing any calculations.

The previous equations for $m_r$ and $\sigma_r$ of the CCD by adding the pre-stress term, can be rewritten like this:

$$\sigma_r = -z\left(D_{11}\frac{\partial^2 w}{\partial r^2} + \frac{1}{r^2}D_{12}\left(r\frac{\partial w}{\partial r} + \frac{\partial^2 w}{\partial \theta^2}\right) + \alpha_T \frac{\Delta T}{h} + D_{11}\sigma_0\right) \tag{16}$$

$$m_r = \int_{-(h/2)}^{+(h/2)} \sigma_r z dz = -\left[D_{11}\frac{\partial^2 w}{\partial r^2} + \frac{1}{r^2}D_{12}\left(r\frac{\partial w}{\partial r} + \frac{\partial^2 w}{\partial \theta^2}\right) + \alpha_T \frac{\Delta T}{h}\right] + D_{11}\frac{h^3\sigma_0}{12} \tag{17}$$

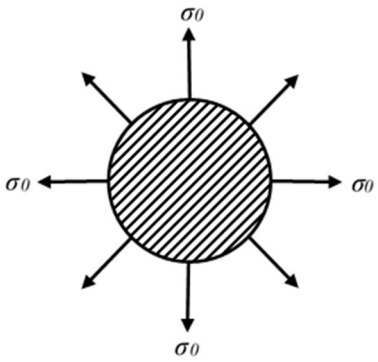


**Figure 6.** The pre-stressing of the diaphragm model.

### 3.4. Solution methodology

If the forces applied and the end supports of the circular diaphragm don't depend on the angle $\varphi$ (see **Figure 5b**). The way the diaphragm bends and the resulting stresses will only depend on the radial position $r$. This kind of bending is called axially symmetrical, which allows us to make some useful simplifications:

$$\frac{\partial^k ()}{\partial \theta^k} = m_{rt} = q_t = 0; \quad k = 1,2,3,4 \tag{18}$$

where $\frac{\partial^k ()}{\partial \theta^k}$ denotes the $k^{th}$ order partial derivative of a function (represented by the

empty parenthesis) with respect to the $\theta$-direction.

Equation (11) shows the key partial differential equation that outlines how a CCD bends under axisymmetric thermal and mechanical loads. Here, $w$ stands for the deflection of the diaphragm along the axial direction. To determine this deflection, the partial differential equation needs to be solved.

To find the exact solution for Equation (11), just add the complementary solution from the related homogeneous differential equation, called $w_h$, to the particular solution, $w_p$.

$$w = w_h + w_p \tag{19}$$

The complementary solution for Equation (11) here:

$$w_h = C_1 \ln r + C_2 r^2 \ln r + C_3 r^2 + C_4 \tag{20}$$

The constants $C_i\,(i = 1,2,3,4)$ can be determined based on the boundary conditions (BCs). the particular solution, $w_p$, can be found by integrating Equation (11) step by step.

$$w_p = \int \frac{1}{r} \int r \int \frac{1}{r} \int \frac{r(P(r)+P_T(r))}{D} drdrdrdr \tag{21}$$

The constraints for the circular film with a clamped edge, as illustrated in **Figure 5**, are:

$$\left.\begin{array}{l} w = 0|_{r=a} \\ \frac{\partial w}{\partial r} = 0\Big|_{a=0} \end{array}\right\} \tag{22}$$

Looking at the circular plate, which doesn't have any concentrated loads right at $r = 0$. The logarithmic terms in Equation (19) lead to infinite displacement and bending moment. The shear force behaves similarly for all values of $C_1$ and $C_2$, except when they're zero, which means that they are set $C_1 = C_2 = 0$. So, when considering a circular plate under an axisymmetric distributed load with any type of boundary conditions, the deflection surface ends up being:

$$w = C_3 r^2 + C_4 + w_p \tag{23}$$

The constants of integration is figured out, $C_3$ and $C_4$, based on the boundary conditions, after making some adjustments, the transverse deflection $w$, along with the bending moments ($m_r$, $m_t$) and shear forces ($q_r$), will look like this:

$$w = \psi_3 P \alpha_T \frac{T_t - T_b}{64 h_o}(a^2 - r^2)^2 + \frac{\psi_1 m_T}{4} r^2 (\ln r - \ln a) + \frac{\psi_2 m_T}{8}(a^2 - 3r^2) \tag{24}$$

$$m_r = \psi_3 P \alpha_T \frac{T_t - T_b}{16 h_o}(a^2 - r^2) + \frac{m_T}{2}(\ln a - \ln r)(\psi_1 - \psi_2) + \frac{\psi_1 h^3 \sigma_0}{12} \tag{25}$$

$$m_t = \psi_3 P \alpha_T \frac{T_t - T_b}{12 h_o}(a^2 - r^2) + \frac{m_T}{2}(\ln a - \ln r)(\psi_1 - 2\psi_2) \tag{26}$$

$$q_r = P \alpha_T \frac{T_t - T_b}{12 h_o}(a^2 - r^2) \tag{27}$$

### 3.5. The structural-thermal field modeling

The structural-thermal field operates on a few key ideas: each field forms independently in solid and mesh models, A rectangular 4-node element type is used, and the total count of elements and nodes is 441 and 400, respectively, with a mesh size of 14 mm. The switching load transmission diagram can be seen in **Figure 7**. This setup leads to a relationship where the volumetric load transfer between the two fields results in a shift of the thermal field due to temperature transfer. On the other hand, when the thermal field changes, it prompts a movement in the structural field through displacement transfer.


**Figure 7.** The Structural-Thermal Field Modeling.

**Figure 8** illustrates the structural-thermal field solver (STFS) algorithm. The duration of the time step in the STFS problem corresponds directly to the time cycle. Throughout the conversion cycle, the fields in the STFS solution connect in an implicit way, and the field cycle incorporates each solution as well as the transfer of volumetric load among the fields. The geometric layout of the CCD structure is depicted in **Figures 9a,b**.

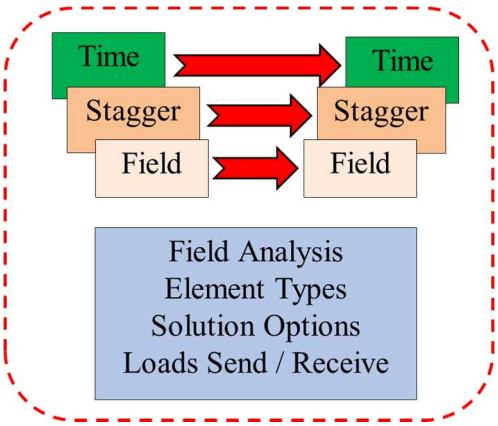


**Figure 8.** Algorithm of STFS via ANSYS.

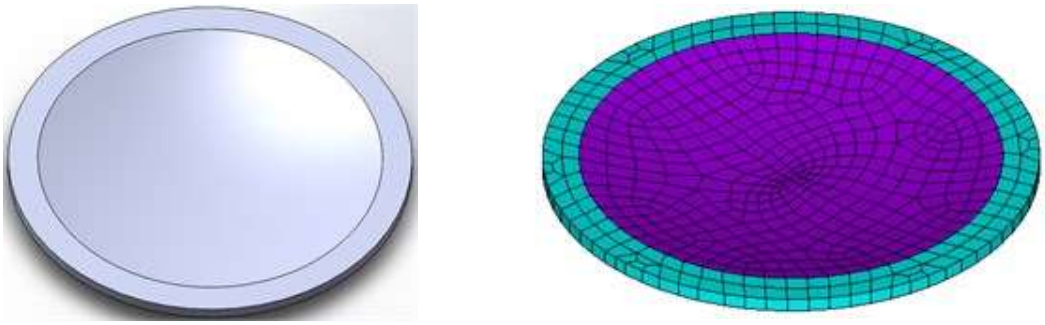

(**a**) A FEM of CCD (**b**) CCD Boundary conditions

**Figure 9.** CCD Geometrical model.

## 4. Result and discussion

### 4.1. The diaphragm model overview

This part presents some numerical results for a CCD that has a geometry of $2a = 1$ mm and a thickness of about 0.1 mm (check **Section 3**). First, the diaphragm is pre-stressed with radial stress $\sigma_0$ and then secured between two plates. Check out **Tables 1 and 2** for its mechanical and thermal properties. Then, **Table 3** outlines the mechanical and thermal loading history applied to the CCD. For this work, a finite element network is selected to suit each of the Multi-Physics fields. Specifically, SHELL 181 is picked for structural analysis, and SOLID87 for thermal applications. The FEM results are set up using ANSYS software.

In this study, the BFRP used here is a novel material for MEMS and bioengineering applications. Selecting laminates, stacking and orientation in composite materials involves arranging individual plies at different angles (commonly $0°, \pm 45°, 90°$) to tailor structural properties like stiffness, strength, and weight to specific loading conditions. The process requires balancing mechanical requirements with manufacturing constraints to avoid defects like delamination or warping.

- 0° Plies: Used to resist axial tension and compression loads.
- $\pm 45°$ Plies: Essential for resisting shear loads and improving torsion resistance.
- 90° Plies: Provide transverse strength and stiffness.

In this study, selected laminates, Cross-Ply composites with a stacking distribution of the CCD are $[0°, 90°, 0°, 90°, 0°]_S$ used for superior damage resistance in bidirectional loading scenarios that suitable in our case. Each ply has 0.02 mm thickness, the volume fraction $V_f = 0.53$

**Table 1.** The BFRP Mechanical properties [28].

| $E_1$ (GPa) | $E_2$ (GPa) | $E_3$ (GPa) | $\upsilon_{12}$ | $\upsilon_{23}$ | $\upsilon_{13}$ | $G_{12}$ (GPa) | $G_{23}$ (GPa) | $G_{13}$ (GPa) |
|---|---|---|---|---|---|---|---|---|
| 93.5 | 20 | 20 | 0.28 | 0.3 | 0.28 | 2.35 | 8.5 | 2.35 |

**Table 2.** The BFRP Thermal properties [28].

| $K_1$ | $K_2$ | $K_3$ | $\alpha_1$ | $\alpha_2$ | $\alpha_3$ | $K_{12}$ | $K_{23}$ | $K_{13}$ |
|---|---|---|---|---|---|---|---|---|
| | $(W \cdot m^{-1} \cdot K^{-1})$ | | | $(K^{-1})$ | | | $(W \cdot m^{-1} \cdot K^{-1})$ | |
| 0.18 | 0.08 | 0.08 | $6E-6$ | $8E-6$ | $6E-6$ | 0.628 | 0.628 | 0.628 |

**Table 3.** The History of Thermo-Mechanical Loading.

| $P\ (MPa)$ | $P_1 = 100$ | $P_2 = 200$ | $P_3 = 300$ | $P_4 = 400$ |
|---|---|---|---|---|
| $T_b\ (C°)$ | $T_1 = 50$ | $T_2 = 100$ | $T_3 = 150$ | $T_4 = 200$ |

### 4.2. The mode shapes of the CCD

Using ANSYS, a static analysis of the dome-shaped diaphragm is applied, followed by a modal analysis. This allowed us to gather the natural frequencies and mode shapes for the first four modes. **Figure 10** presents the first four mode shapes of the CCD.

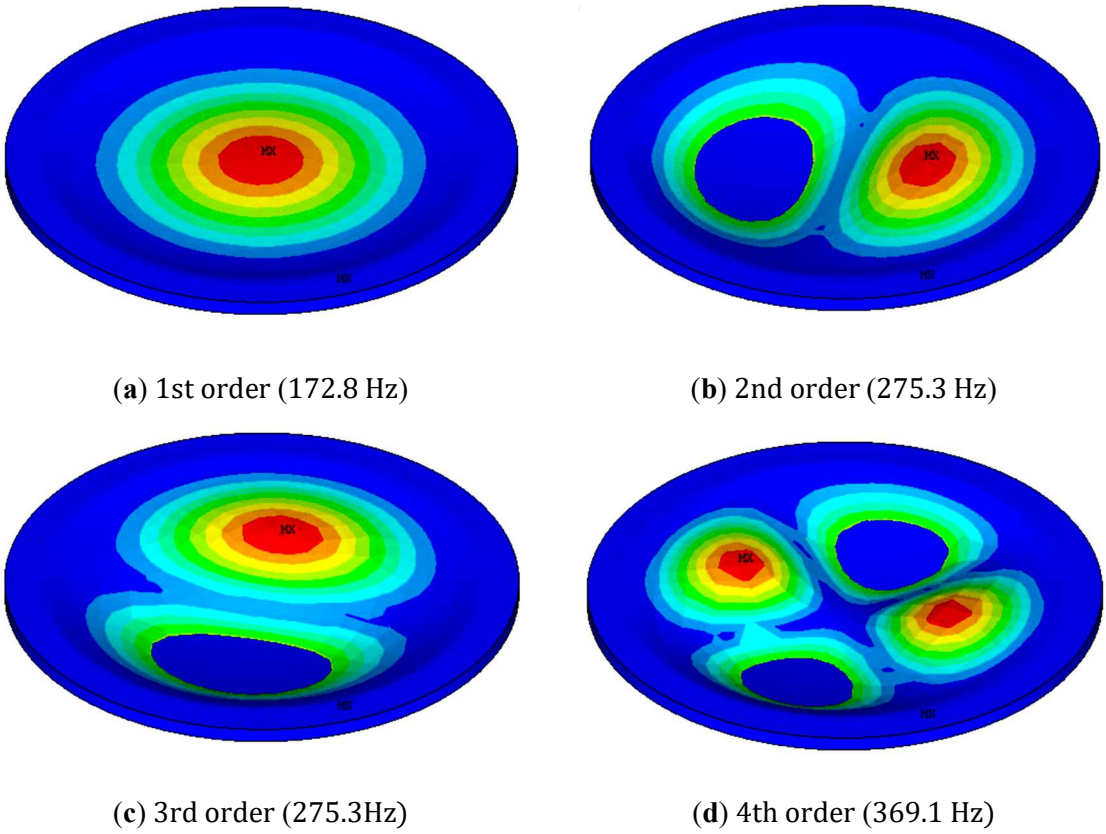

(**a**) 1st order (172.8 Hz) (**b**) 2nd order (275.3 Hz)

(**c**) 3rd order (275.3Hz) (**d**) 4th order (369.1 Hz)

**Figure 10.** The first four mode shapes of the CCD.

### 4.3. The Thermal Model for BFRP diaphragm

The thermal effect equation for BFRP materials by tracking the cumulative deterioration index of diaphragm material can be described using various related parameters (where the properties of BFRP are presented in **Table 4**):

$$D = \left\{\left(1-\frac{F}{E_c(T)}\right)(1-f^*)\frac{ln(N+1)}{ln(nN_f)}\right\} + \left\{\left(1-\frac{F}{E_c(T)}\right)f^*\left(\frac{N}{nN_f}\right)\right\} + \left\{\frac{F}{E_c(T)}\left(1-\frac{\sigma_{max}(1-R)}{2\sigma_{ult}(T)}\right)\frac{ln\left(1-\frac{N}{nN_f}\right)}{ln\left(\frac{1}{nN_f}\right)}\right\} \quad (28)$$

**Table 4.** BFRP Parameters list [28].

| Parameter | BFRP |
|---|---|
| Fatigue Life $N_f$ | $6.12 \times 10^4$ |
| Young's Modulus of Matrix $E_m$(GPa) | 4.06 |
| Volume Fraction of Matrix $V_m$ | 0.43 |
| Young's Modulus of Fiber $E_f$(GPa) | 97 |
| Volume Fraction of Fiber $V_f$ | 0.53 |
| Young's Modulus of Composite $E_c$(GPa) | 84 |
| Polymer Melting Point $T_m$(°K) | 446 |
| Fiber-Matrix Interface Strength $f^*$ | 0.52 |
| fatigue stress $S_f$(MPa) | 137 |
| Ultimate Tensile Stress $S_{ult}$(MPa) | 1409 |

| | |
|---|---|
| Minimum Fatigue Stress $\sigma_{min}$(MPa) | 14.2 |
| Maximum Fatigue Stress $\sigma_{max}$(MPa) | 139 |
| Stress Ratio $R$ | 0.10 |
| Percentage of Drop in Stiffness $n$ | 1.66 |

Looking at **Figure 11a,b**, can see that the thermal cumulative deterioration relationship for the diaphragm material holds true to Equation (28). It shows that the lower side of the diaphragm is the most vulnerable to thermal effects, reaching a maximum temperature of $T_L = 333.15K$. Meanwhile, the upper side registers the lowest at $T_U = 293.15K$. As we get closer to the melting point, the rate of deterioration really starts to ramp up.

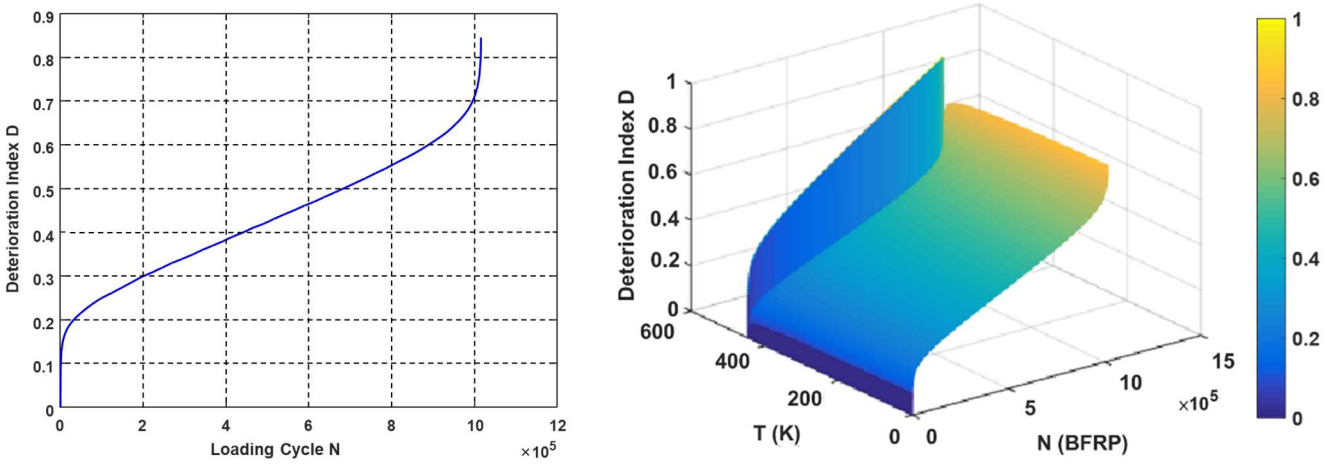


(**a**) D-N relationship (**b**) D-T-N relationship

**Figure 11.** The Thermal Model for BFRP.

## 4.4. The analytical and numerical analysis for CCD

### 4.4.1. The mechanical behavior of CCD

Herein, the mechanical behavior of CCD under the previously mentioned conditions can see at **Figures 12–15**. The mechanical behavior, such as transverse deflection ($w$), bending moments ($m_r$, $m_t$), shear force ($q_r$), and stress ($S_r$, $S_t$) distributed over the CCD radius ($r$) with different pressures ($P$) are shown in **Figures 12–14**. **Figure 12** shows that as the CCD radius ($r$) gets larger, the transverse deflection ($w$) decreases, while it actually increases with pressure ($P$), peaking at the center of the CCD when $r = 0$. Then, in **Figure 13** there are diagrams of the bending moments, both radial and tangential, and shear force, which rise with increasing pressure ($P$). The residual moment from pre-stress moment affect is shown clear in in **Figure 13a**, and the maximum bending moments ($m_r$, $m_t$) appear at ($r = a, r = 0$) respectively. Moving on to **Figure 13c**, it shows that the shear force ($q_r$) increases with both the CCD radius and the pressure, reaching its peak at the edge of the CCD when $r = a$. Lastly, **Figure 14** presents the stress in the radial and tangential directions of the CCD, which also increases with pressure ($P$), and the pre-stress value is shown in **Figure 14a**.

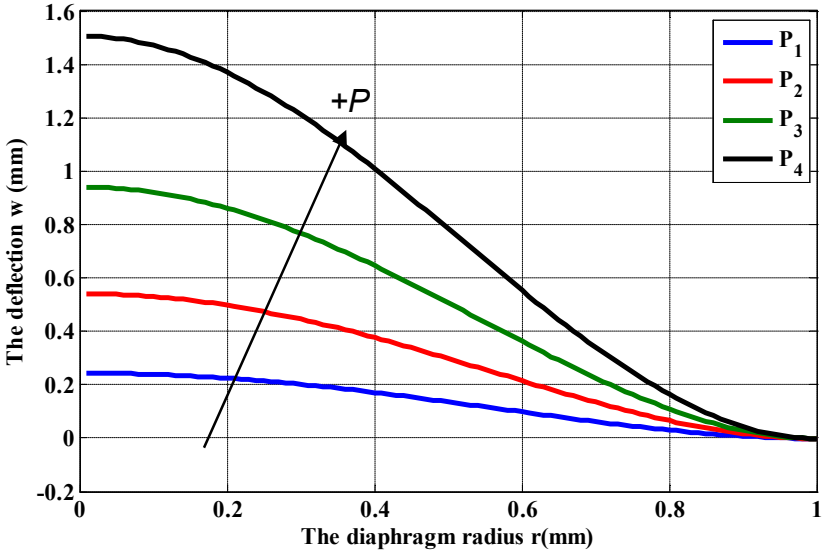


**Figure 12.** The diaphragm Transverse deflection $w$ over the radius ($r$) under varying Pressure (P).

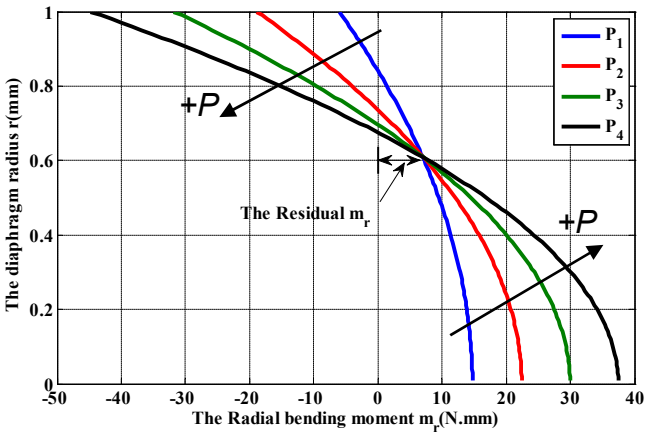


(**a**) Radial bending moment $m_r$

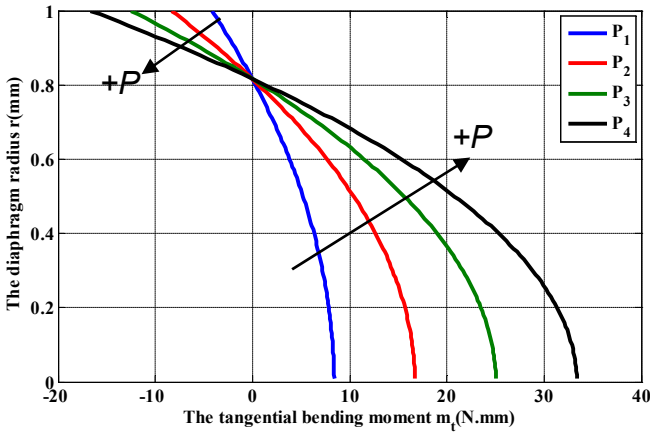


(**b**) Tangential bending moment $m_t$

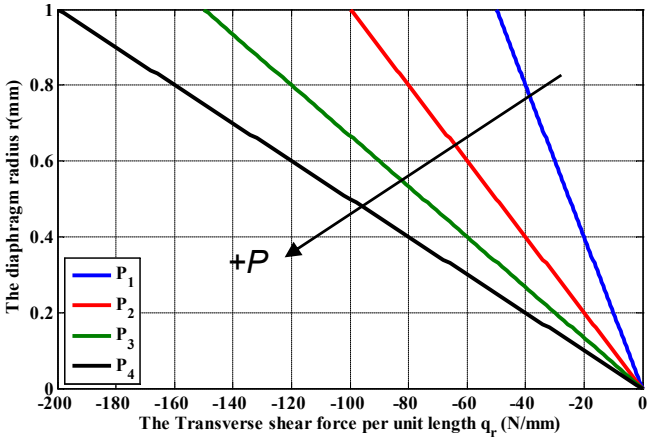


(**c**) Shear force $q_r$

**Figure 13.** The diaphragm bending moment and Shear force over the radius ($r$) under varying Pressure (P).

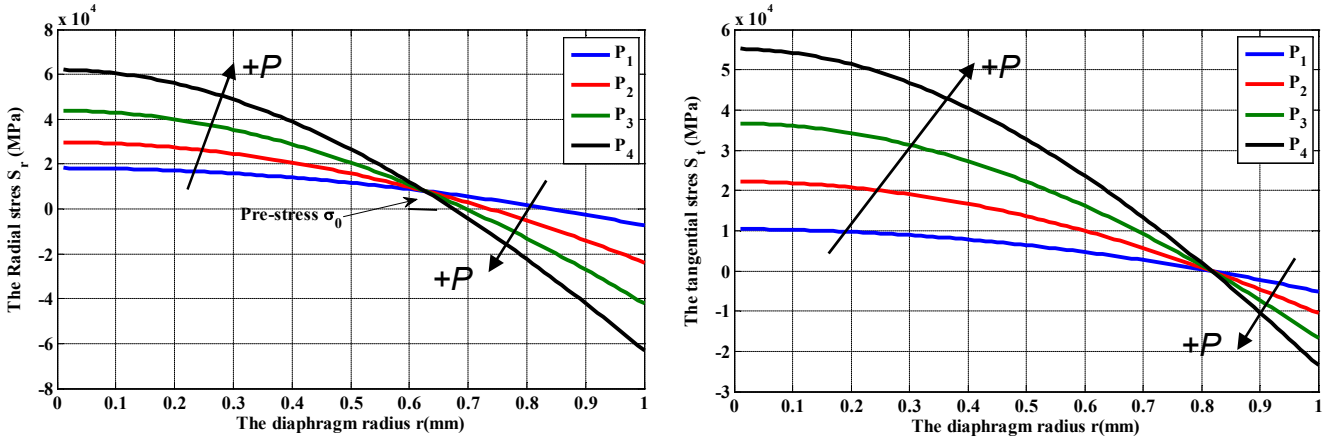


(**a**) Radial stress $S_r$ (**b**) Tangential stress $S_t$

**Figure 14.** The diaphragm stress disteribution over the radius ($r$) under varying Pressure (P).

**Figure 15** illustrates how radial stress $S_r$ affects radial strain $e_r$, showing that as the radial stress increases, so does the radial strain. This relationship is crucial in engineering analysis since it can determine $E$ of the CCD material from the slope of this linear connection.

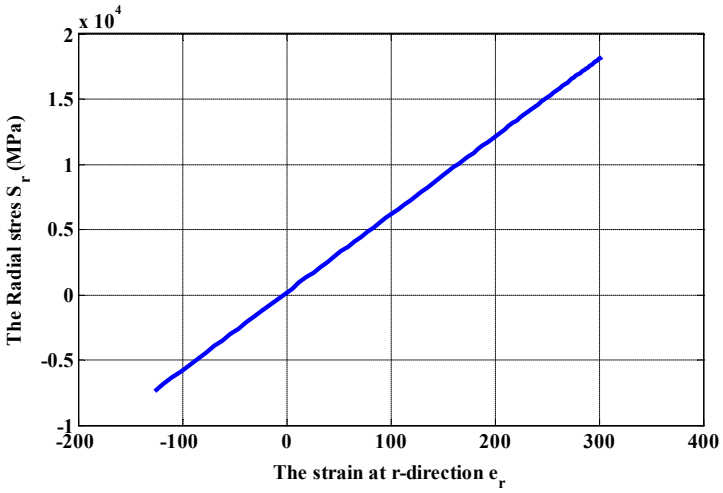


**Figure 15.** The diaphragm radial stress $S_r$ and radial strain $e_r$ relationship.

### 4.4.2. The thermal behavior of CCD

The thermal behavior of the CCD based on the earlier conditions is shown in **Figure 16**. The bending moments ($m_r$, $m_t$) distributed over the CCD radius ($r$) as the temperature ($T_b$) changes are shown in **Figure 16a,b**. It's interesting to note that the maximum bending moments rise as the temperature increases.

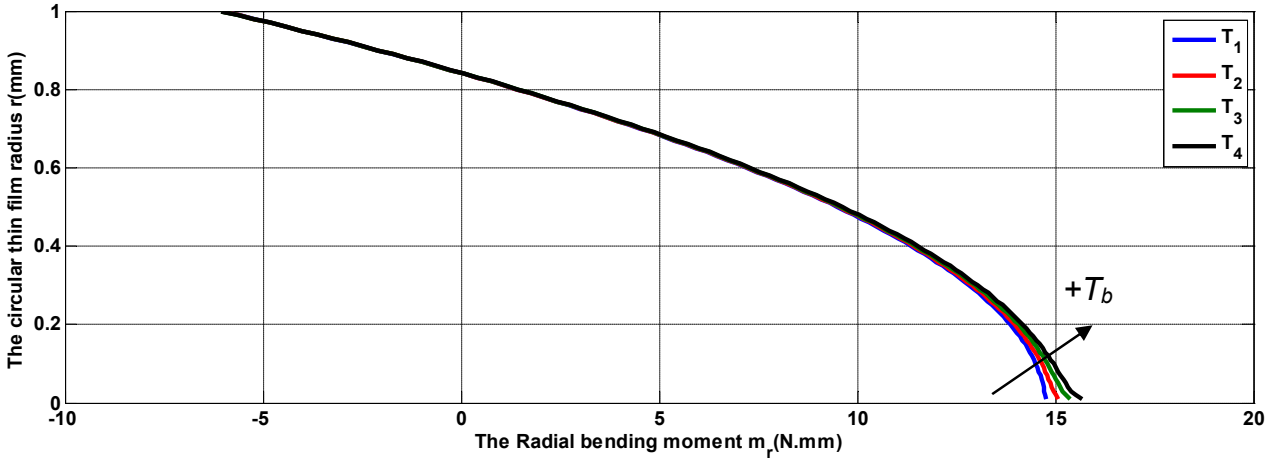


(**a**) $m_r$

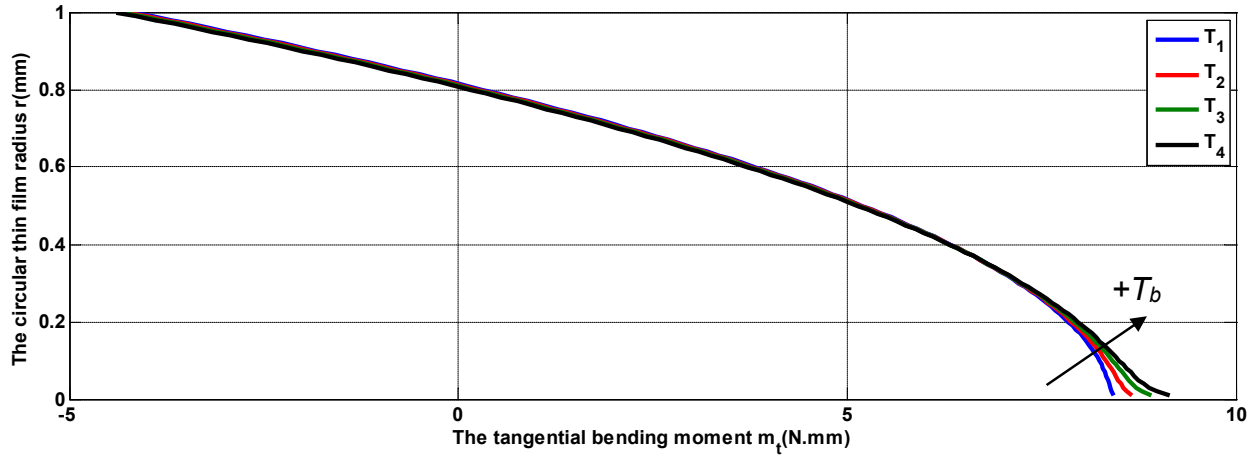


(**b**) $m_t$

**Figure 16.** The diaphragm bending moment over the radius ($r$) under varying temperature ($T_b$).

### 4.4.3. The thermo-mechanical behavior of CCD

**Figure 17** illustrates how the thickness of the CCD deforms from the center to the edge ($r$) when pressure ($P$) and temperature ($T_b$) change. As shown in **Figure 17a**, the thickness of the dome (h) increases as move out from the center (r) but decreases when pressure ($P$) goes up. In **Figures 17b,c**, the thickness strain ($e_h$) rises with both pressure ($P$) and temperature ($T_b$).

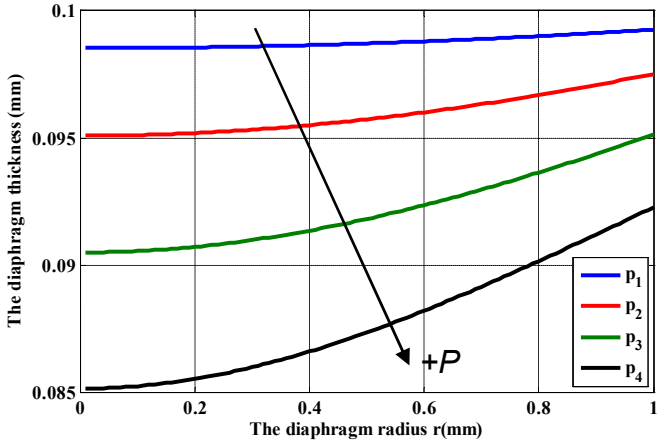


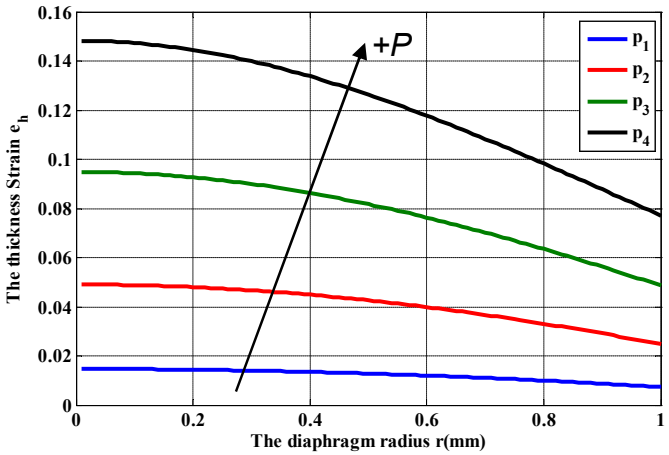

(**a**) $h$ vs $r$ with varying $P$ (**b**) $e_h$ vs r with varying $P$

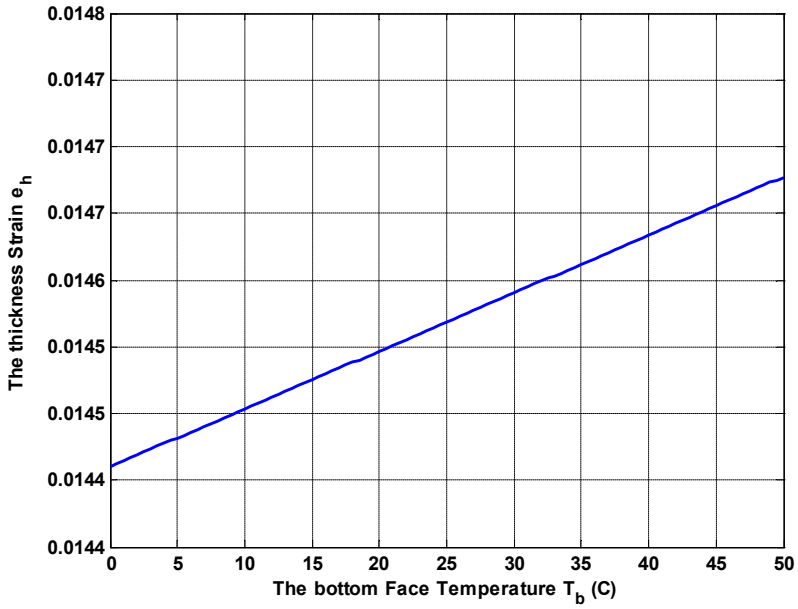


(**c**) $e_h$vs $T_b$

**Figure 17.** The diaphragm thickness ($h$) and thickness. strain $e_h$ behaviour under different pressures ($P$) and temperatures ($T_b$).

**Figure 18** illustrates how the CCD deforms under a pressure of $P = P_1 =$ 100 MPa and $T_b = T_1 = 50$ numerically using ANSYS software, showing the 3D contour mode. From the figure, the highest deflection happens at the center of the CCD, specifically at $r = 0$, where the maximum deflection $w_{max}$ reaches 0.24 mm. When comparing the maximum deflection from the FEM with the results from analytical calculations, the results are quite close to each other.

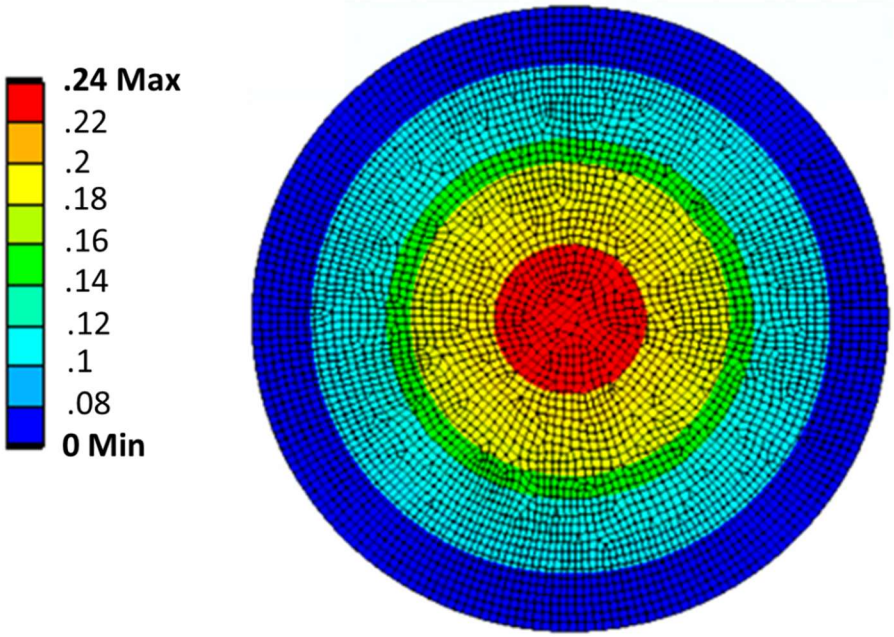


**Figure 18.** The Numerical results of diaphragm deformation $w_{max}$ at $P_1$, and $T_1$.

### 4.5. Accuracy and reliability evaluation of the current analysis for CCD

To calculate the error between analytical and numerical results to evaluate the accuracy and reliability of the current analysis for CCD, the two metrics are used: absolute error and relative error. These methods quantify how close the numerical solution is to the true analytical solution.

The absolute error measures the raw numerical difference between the true value and the approximate value. It provides the magnitude of the error in the same units as the measured quantity, like this:

$$E_a = \left|X_{analytical} - X_{numerical}\right| \tag{29}$$

where $X_{analytical}$ is the analytical solution and $X_{numerical}$ as a numerical solution.

The relative error provides a better sense of the error's significance by comparing the absolute error to the size of the true value. It is a dimensionless value and is often expressed as a percentage (percentage error), like this:

$$E_r = \frac{\left|X_{analytical} - X_{numerical}\right|}{\left|X_{analytical}\right|} \times 100 \tag{30}$$

**Figure 19** presents the relative error ($E_r$) between analytical and numerical results, the relative error is less than 0.3% for $w_{max}$ between analytical and numerical results under pressure ($P$) and temperature ($T_b$). Therefore, the present analysis for CCD gave a good agreement for the numerical results, even for $w_{max}$ of CCD.

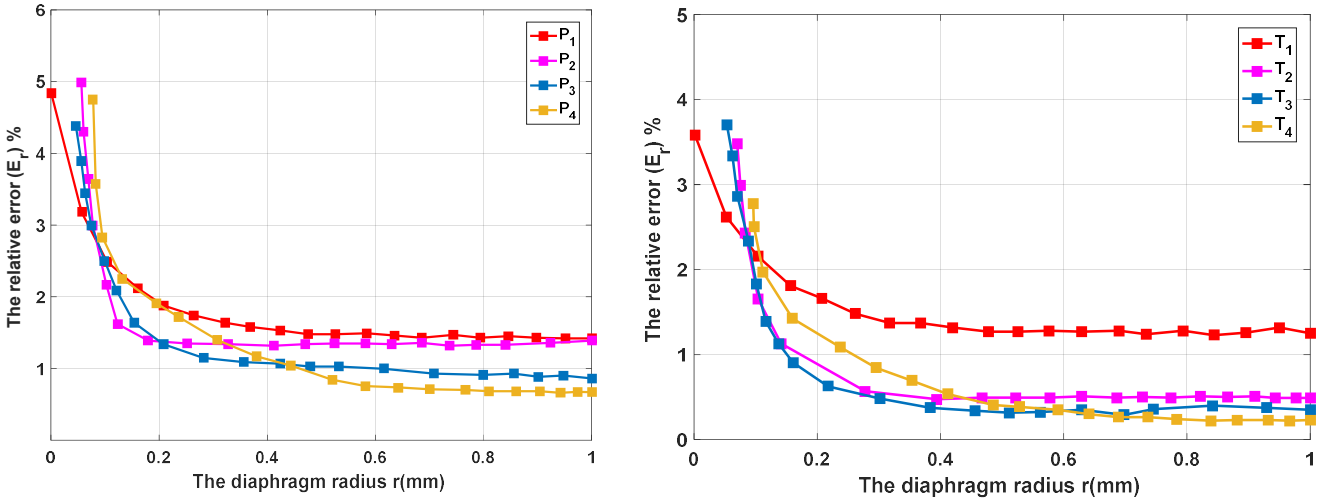


(**a**) Under various pressures ($P$) (**b**) Under various temperatures ($T_b$)

**Figure 19.** The relative error ($E_r$) between analytical and numerical results for maximum deformation $w_{max}$.

## 5. Conclusion

This paper presents a thorough analysis of the BT technique for CCD made from BFRP under thermal and mechanical loads. First, the partial differential equation has been derived for the diaphragm through analytical methods. Next, the mechanical and thermal flow curves for the material were plotted and discussed using MATLAB and its PDE toolbox. The thermal cumulative deterioration relationship was plotted by deriving the thermal effect equation for BFRP materials by tracking the cumulative

deterioration index of the diaphragm material, using various BFRP parameters. The first four mode shapes of the CCD were also plotted, and the thickness distribution across the radius of the diaphragm was used to understand its mechanical behavior when deformed. Moreover, an FEM was conducted for the BT using ANSYS software, aligning with the conditions used in our analytical calculations. A comparison was made between the two methods to assess their accuracy and validity, and the relative error ($E_r$) for $w_{max}$ between the analytical and numerical results was found to be less than 0.3%, indicating FEM converges well with the analytical model based on our results.

**Conflict of interest:** The author declare no conflicts of interest to report regarding the present study.

**Abbreviations**

| | |
|---|---|
| BT | Bulge test |
| CCD | Composite circular diaphragms |
| MEMS | Microelectromechanical sensors |
| BFRP | Basalt fiber reinforced polymer |
| FEM | Finite element model |
| STFS | Structural-thermal field solver |
| PDE | Partial differential equation |
| $E_r$ | Relative error |
| $P$ | Pressure |
| $T_b$ | Bottom surface temperature |
| $T_t$ | Top surface temperature |
| $a$ | The diaphragm radius |
| $h$ | The diaphragm thickness |
| $w(r,\theta,t)$ | The diaphragm deflection |
| $w$ | The transverse deflection |
| $m_r, m_t, m_{rt}$ | The moments of bending and twisting |
| $q_r, q_t$ | The shear forces |
| $S_r, S_t$ | The stresses |
| $e_r, e_t$ | The strain |
| $e_h$ | The thickness strain |
| $\rho$ | The density per unit area of the diaphragm |
| $R$ | The radius of curvature |
| $D_{ij}$ | The diaphragm's flexural rigidity |
| $\bar{Q}_{ij}$ | The stiffness coefficient |
| $\bar{N}_r, \bar{N}_\theta$ and $\bar{N}_{r\theta}$ | In-plane force |
| $P_T$ | Applied Pressure |
| $\Omega$ | The non-dimensional frequency parameter |
| $\omega$ | The natural frequency |
| $\sigma_0$ | The biaxial residual stress per unit length |
| $w_{max}$ | The Maximum deflection |
| $E_1, E_2, E_3$ | The elastic modulus in the '1', '2' and '3' directions respectively |
| $G_{12}, G_{23}, G_{13}$ | The shear modulus in the '1-2', '2-3' and '1-3' planes respectively |
| $\nu_{12}, \nu_{23}, \nu_{13}$ | The Poisson's ratio in the '1-2', '2-3' and '1-3' Planes respectively |
| $K_1, K_2, K_3$ | The thermal conductivity in the '1', '2' and '3' directions respectively |
| $\alpha_1, \alpha_2, \alpha_3$ | The thermal expansion coefficient in the '1', '2' and '3' directions respectively |
| $K_{12}, K_{23}, K_{13}$ | The thermal conductivity in the '1-2', '2-3' and '1-3' plane respectively |

| | |
|---|---|
| $N_f$ | Fatigue Life |
| $E_m$(GPa) | Young's Modulus of Matrix |
| $V_m$ | Volume Fraction of Matrix |
| $E_f$(GPa) | Young's Modulus of Fiber |
| $V_f$ | Volume Fraction of Fiber |
| $E_c$(GPa) | Young's Modulus of Composite |
| $T_m(°K)$ | Polymer Melting Point |
| $f^*$ | Fiber-Matrix Interface Strength |
| $S_f$(MPa) | fatigue stress |
| $S_{ult}$(MPa) | Ultimate Tensile Stress |
| $\sigma_{min}$(MPa) | Minimum Fatigue Stress |
| $\sigma_{max}$(MPa) | Maximum Fatigue Stress |
| $n$ | Percentage of Drop in Stiffness |
| $E_a$ | The absolute error |
| $E_r$ | The relative error |
| $\xi$ | The value of Tsai-Wu damage criterion |
| $C_{xy}, C_{yz}, C_{xz}$ | The coupling coefficient for Tsai-Wu theory |
| $\sigma_x, \sigma_y, \sigma_z$ | The local stress components in directions $(x)$, $(y)$, and $(z)$ |
| $\sigma_{xy}, \sigma_{yz}, \sigma_{xz}$ | The local shear components |
| $\sigma_{xt}^f, \sigma_{yt}^f, \sigma_{zt}^f$ | The local tension and compression strength components in directions $(x)$, $(y)$, and $(z)$ |
| $\sigma_{xc}^f, \sigma_{yc}^f, \sigma_{zc}^f$ | The local shear strength component |
| $F_x$ , $F_y$ | The local strength components in directions $(x)$ and (y), respectively |
| $F_{xy}$ | The local shear strength component. |

# Appendix A

**Table A1.** Failure criteria of the composite materials [3,4].

| No. | Failure criteria | Mathematical formula |
|---|---|---|
| 1 | Max. stress | $\sigma_x = F_x$ , $\sigma_y = F_y$, $\sigma_{xy} = F_{xy}$ |
| 2 | Max. strain | $\sigma_x = F_x + \upsilon_{xy}\sigma_y$ , $\sigma_y = F_y + \upsilon_{xy}\frac{E_y}{E_x}\sigma_x$, $\sigma_{xy} = F_{xy}$ |
| 3 | Tsai-Wu | If the criterion used is the "strength index": $\xi = A + B$ And if the criterion used is the inverse of the "strength ratio": $\xi = 1.0/\left(-\frac{B}{2A} + \sqrt{(B/2A)^2 + 1.0/A}\right)$ where: $\xi$ = value of Tsai-Wu failure criterion: $A = -\frac{(\sigma_x)^2}{\sigma_{xt}^f\sigma_{xc}^f} - \frac{(\sigma_y)^2}{\sigma_{yt}^f\sigma_{yc}^f} - \frac{(\sigma_z)^2}{\sigma_{zt}^f\sigma_{zc}^f} + \frac{(\sigma_{xy})^2}{(\sigma_{xy}^f)^2} + + \frac{(\sigma_{yz})^2}{(\sigma_{yz}^f)^2} + \frac{(\sigma_{xz})^2}{(\sigma_{xz}^f)^2} + \frac{C_{xy}\sigma_x\sigma_y}{\sqrt{\sigma_{xt}^f\sigma_{xc}^f\sigma_{yt}^f\sigma_{yc}^f}} + \frac{C_{yz}\sigma_y\sigma_z}{\sqrt{\sigma_{yt}^f\sigma_{yc}^f\sigma_{zt}^f\sigma_{zc}^f}} + \frac{C_{xz}\sigma_x\sigma_z}{\sqrt{\sigma_{xt}^f\sigma_{xc}^f\sigma_{zt}^f\sigma_{zc}^f}}$ $B = \left(\frac{1}{\sigma_{xt}^f} + \frac{1}{\sigma_{xc}^f}\right)\sigma_x + \left(\frac{1}{\sigma_{yt}^f} + \frac{1}{\sigma_{yc}^f}\right)\sigma_y + \left(\frac{1}{\sigma_{zt}^f} + \frac{1}{\sigma_{zc}^f}\right)\sigma_z$ $C_{xy}, C_{yz}, C_{xz} = x-y, y-z, x-z$, respectively. |
| 4 | Hashin Fiber and Matrix | Fiber Failure Criterion $\xi = \begin{cases} \left(\frac{\sigma_x}{\sigma_{xt}^f}\right)^2 + \frac{\sigma_{xy}^2+\sigma_{xz}^2}{\left(\sigma_{xy}^f\right)^2} & \sigma_x > 0 \\ \left(\frac{\sigma_x}{\sigma_{xc}^f}\right)^2 & \sigma_x \le 0 \end{cases}$ |

Matrix Failure Criterion

$$\xi = \begin{cases} \left(\frac{\sigma_y + \sigma_z}{\sigma_{yt}^f}\right)^2 + \frac{\sigma_{yz}^2 - \sigma_y\sigma_z}{\left(\sigma_{yz}^f\right)^2} + \frac{\sigma_{xy}^2 + \sigma_{xz}^2}{\left(\sigma_{xy}^f\right)^2} & \sigma_y + \sigma_z > 0 \\ \frac{1}{\sigma_{yc}^f}\left(\left(\frac{\sigma_{yc}^f}{2\sigma_{yz}^f}\right)^2 - 1\right)(\sigma_y + \sigma_z) + \left(\frac{\sigma_y + \sigma_z}{2\sigma_{yz}^f}\right)^2 + \frac{\sigma_{yz}^2 - \sigma_y\sigma_z}{\left(\sigma_{yz}^f\right)^2} + \frac{\sigma_{xy}^2 + \sigma_{xz}^2}{\left(\sigma_{xy}^f\right)^2} & \sigma_y + \sigma_z \le 0 \end{cases}$$

These criteria are employed for fatigue development, damage simulation, and stress analysis.

## References


1. Altabey WA. The fatigue damage monitoring of composite pipeline based on frequency domain analysis of electrical capacitance sensor system measurements. International Journal of Lightweight Materials and Manufacture. 2025; 8(6): 779-792. doi: 10.1016/j.ijlmm.2025.06.002
2. Altabey WA. A novel framework to identify delamination location/size in BFRP pipe based on convolutional neural network (CNN) algorithm hybrid with capacitive sensors. International Journal of Lightweight Materials and Manufacture. 2025; 8(3): 393-401. doi: 10.1016/j.ijlmm.2024.12.002
3. Altabey WA. An Artificial Intelligence-Based Scheme for Structural Health Monitoring in CFRE Laminated Composite Plates under Spectrum Fatigue Loading. Structural Durability & Health Monitoring. 2025; 19(5): 1145-1165. doi: 10.32604/sdhm.2025.068922
4. Altabey WA. The Laminated Pipeline Material Delamination Identification Based on Artificial Intelligence Schemes. Advances in Machinery, Materials Science and Engineering Application X. Published online October 17, 2024. doi: 10.3233/atde240713
5. Rossi M, Lattanzi A, Barlat F, et al. Inverse identification of large strain plasticity using the hydraulic bulge-test and full-field measurements. International Journal of Solids and Structures. 2022; 242: 111532. doi: 10.1016/j.ijsolstr.2022.111532
6. Shchemelinin Y, Nelson JW, Ryan C, et al. Hydraulic bulge forming comparison of continuous and stretch broken carbon fiber prepreg laminates. Composites Part B: Engineering. 2025; 303: 112607. doi: 10.1016/j.compositesb.2025.112607
7. Shchemelinin Y, Nelson JW, Ryan C, et al. Hydraulic bulge testing to compare formability of continuous and stretch broken carbon fiber reinforced polymer composites. International Journal of Material Forming. 2023; 16(2). doi: 10.1007/s12289-023-01743-6
8. Xiang Y, Chen X, Vlassak JJ. Plane-strain Bulge Test for Thin Films. Journal of Materials Research. 2005; 20(9): 2360-2370. doi: 10.1557/jmr.2005.0313
9. Boyer A, Demazel N, Coër J, et al. A novel hydraulic bulge test in hot forming conditions. Journal of Materials Processing Technology. 2023; 316: 117917. doi: 10.1016/j.jmatprotec.2023.117917
10. Hill R. C. A theory of the plastic bulging of a metal diaphragm by lateral pressure. The London, Edinburgh, and Dublin Philosophical Magazine and Journal of Science. 1950; 41(322): 1133-1142. doi: 10.1080/14786445008561154
11. Mellor PB. Stretch forming under fluid pressure. Mechanics and Physics of Solids. 1956; 5(1), 41–56.
12. Suleman K, Bosi F. Finite strain elastoplastic bulging of circular diaphragms. International Journal of Solids and Structures. 2023; 267: 112148. doi: 10.1016/j.ijsolstr.2023.112148
13. Ashrafian MM, Hosseini Kordkheili SA. Plastic temperature-dependent constitutive modeling of pure aluminum diaphragms at large strains by using bulge test. Journal of Materials Research and Technology. 2021; 11: 412-427. doi: 10.1016/j.jmrt.2021.01.022
14. Shi J, Guo ZJ, Wang JX, et al. A novel small specimen testing method based on a pneumatic bulging test: Measurement of tensile properties at high temperatures. International Journal of Pressure Vessels and Piping. 2024; 209: 105210. doi: 10.1016/j.ijpvp.2024.105210
15. Barnwal VK, Lee SY, Choi J, et al. On the fracture characteristics of advanced high strength steels during hydraulic bulge test. International Journal of Mechanical Sciences. 2021; 190: 106032. doi: 10.1016/j.ijmecsci.2020.106032
16. Bao J, Ding H, Zuo Z, et al. Exploring Mechanical Properties Using the Hydraulic Bulge Test and Uniaxial Tensile Test with Micro-Samples for Metals. Metals. 2024; 14(8): 917. doi: 10.3390/met14080917
17. Tian R, Kong X, Liao Z. Two dimensional CFD simulation of rupture process of shock tube diaphragm. Chinese congress of theoretical and applied mechanics. 2022.

18. Currao GMD, Hsu SY. Diaphragm-Induced Attenuation in Shock Tubes. AIAA Journal. 2024; 62 (8), 2862-2875. doi: 10.2514/1.j063847
19. Li T, Gao L, Liu Z, et al. Numerical Analysis of Rupture Process of Large Diameter Diaphragm in a Combined High Enthalpy Wind Tunnel. Aerodynamic Research & Experiment. 2024; 5(1), 86-94, doi: 10.12050/are20220111
20. Wan K, Guo S, Dillard DA. A theoretical and numerical study of a thin clamped circular film under an external load in the presence of a tensile residual stress. Thin Solid Films. 2003; 425, 150–162.
21. Jung BB, Lee HK, Park HC. Measurement of Mechanical Properties of Thin Films Using a Combination of the Bulge Test and Nanoindentation. Transactions of the Korean Society of Mechanical Engineers B. 2012; 36(2): 117-123. doi: 10.3795/ksme-b.2012.36.2.117
22. Yang L, Long S, Ma Z, Wang Z. Accuracy analysis of plane-strain bulge test for determining mechanical properties of thin films. Transactions of Nonferrous Metals Society of China. 2014; 24(10), 3265-3273.
23. Jung BB, Lee HK, Hwang KH, et al. Observation of Size Effect and Measurement of Mechanical Properties of Ti Thin Film by Bulge Test. Transactions of the Korean Society of Mechanical Engineers B. 2013; 37(1): 19-25. doi: 10.3795/ksme-b.2013.37.1.019
24. Grolleau V, Gary G, Mohr D. Biaxial testing of sheet materials at high strain rates using viscoelastic bars. Experimental Mechanics. 2008; 48, 293-306.
25. Zhang JJ, Sun Y yi, Li D sen, et al. Modeling the mechanics of graphene-based polymer composite film measured by the bulge test. Journal of Physics D: Applied Physics. 2015; 48(42): 425302. doi: 10.1088/0022-3727/48/42/425302
26. Huang A, Lu C, Wu S, et al. Viscoelastic Mechanical Properties Measurement of Thin Al and Al-Mg Films using Bulge Testing", Thin Solid Films, 2016; 618: 2-7. doi: 10.1016/j.tsf.2016.03.064.
27. Suttner S, Merklein M. Experimental and numerical investigation of a strain rate controlled hydraulic bulge test of sheet metal. Journal of Materials Processing Technology. 2016; 235: 121-133. doi: 10.1016/j.jmatprotec.2016.04.022
28. Altabey WA. A comprehensive study of a long-term creep thermo-mechanical fatigue behavior monitoring of BFRP composite pipeline using electrical capacitance sensors and deep learning algorithm. International Journal of Fatigue. 2024; 184: 108277. doi: 10.1016/j.ijfatigue.2024.108277